David L. Buckley, PhD
Caleb Roberts, BSc
Geoff J. M. Parker, PhD
John P. Logue, MB, ChB, FRCR
Charles E. Hutchinson, MD, FRCR

Index terms:
Magnetic resonance (MR), tissue characterization, 844.12117, 844.12146
Neoplasms, blood supply, 844.316, 844.32
Prostate neoplasms, MR, 844.12146

Published online before print
10.1148/radiol.2333032098
Radiology 2004; 233:709–715

[1] From Imaging Science and Biomedical Engineering, University of Manchester, Stopford Building, Oxford Road, Manchester M13 9PT, England (D.L.B., C.R., G.J.M.P., C.E.H.); and Department of Clinical Oncology, Christie Hospital, Manchester, England (J.P.L.). Received December 23, 2003; revision requested February 24, 2004; revision received March 18; accepted April 8. Supported by a grant from the U.S. Department of Defense Prostate Cancer Research Program (PC991154). **Address correspondence to** D.L.B. (e-mail: *david.buckley@man.ac.uk*).

Authors stated no financial relationship to disclose.

Author contributions:
Guarantor of integrity of entire study, D.L.B.; study concepts and design, D.L.B., J.P.L., C.E.H.; literature research, D.L.B.; clinical studies, C.E.H., J.P.L.; data acquisition, D.L.B., C.E.H., J.P.L.; data analysis/interpretation, D.L.B., C.R., G.J.M.P., J.P.L.; statistical analysis, D.L.B.; manuscript preparation, D.L.B.; manuscript definition of intellectual content, D.L.B., G.J.M.P., C.E.H.; manuscript editing, D.L.B., G.J.M.P., J.P.L., C.E.H.; manuscript revision/review and final version approval, all authors

Prostate Cancer: Evaluation of Vascular Characteristics with Dynamic Contrast-enhanced T1-weighted MR Imaging—Initial Experience[1]

PURPOSE: To use contrast material–enhanced magnetic resonance (MR) imaging and a distributed-parameter tracer kinetics model for prospectively evaluating the vascular characteristics of prostate cancer.

MATERIALS AND METHODS: Twenty-two patients between 57 and 76 years of age (mean age, 67 years) with histologically proved adenocarcinoma of the prostate were examined by using three-dimensional dynamic contrast-enhanced T1-weighted MR imaging at 1.5 T. The local research ethics committee approved this study, and written consent was obtained from all patients. Data from regions of interest drawn in tumor, normal-appearing peripheral zone tissue, and muscle were analyzed to provide estimates of perfusion, blood volume, interstitial volume, and microvascular permeability–surface area product. These estimates were compared by using the nonparametric Wilcoxon signed rank test.

RESULTS: Mean blood flow was significantly ($P < .001$) higher in 22 prostate tumors than in 20 contralateral peripheral zones (66 vs 32 mL/100 mL/min). Similarly, the interstitial distribution volume in tumors was enlarged compared with the interstitial distribution volume in normal peripheral zones (42 vs 27 mL/100 mL). Blood volume and microvascular permeability–surface area product values in tumors (1.0 mL/100 mL and 22 mL/100 mL/min, respectively) were similar to estimated values in peripheral zone tissue (1.5 mL/100 mL and 21 mL/100 mL/min, respectively).

CONCLUSION: These findings show considerable promise for isolating vascular characteristics of prostate cancer.

Magnetic resonance (MR) imaging remains the most promising technique for the detection and staging of prostate cancer despite its current limitations in sensitivity and specificity (1). Conventional MR imaging, typically performed by using fast T2-weighted spin-echo acquisitions, yields excellent anatomic images of the gland in which the normal peripheral zone and central portion of the gland may be distinguished. However, malignant tissue is not always clearly visualized, particularly when it coexists with benign prostatic hyperplasia in the central gland (2). Although initially considered to be of limited use for studying the prostate (3), contrast material–enhanced MR imaging has shown promise in a series of studies involving the rapid acquisition of early or dynamic data after contrast material administration (4–7). In these studies, cancers (principally in the peripheral zone of the gland) are seen to enhance more rapidly (5) or avidly (7) than normal tissues.

It is likely that the early enhancement seen in cancer is due in part to angiogenesis associated with early tumor growth. The growth of prostate cancer is associated with the development of a rich blood supply fed by a large network of immature, leaky blood vessels (8). The density of this network is related to tumor grade and metastatic potential (9).

Because conventional methods of assessing angiogenesis require the processing of pathologic specimens, there is considerable interest in developing noninvasive tools to assess the microvascular characteristics of prostate cancer in vivo (10).

A link between contrast material uptake in solid tumors and their microvascular characteristics certainly exists, but the precise relationship between tracer kinetics, which are often measured in terms of heuristic measurements, and microvessel density, which is measured at pathologic examination, remains unclear (11,12). The assessment of tracer kinetics in absolute physiologic terms may help to address this question (13). Increasing microvessel density will lead to an increase in blood flow, blood volume, and the surface area of vessel walls. An upturn in vascular endothelial growth factor production is likely to increase the permeability of these vessel walls.

Blood flow, blood volume, and microvascular permeability–surface area product are all, in principle, quantifiable through analysis of contrast-enhanced MR imaging data by using distributed-parameter tracer kinetics models (10,14). To our knowledge, these have yet to be applied in vivo with MR imaging in a substantial patient group, although results of a recent preliminary computed tomography (CT)-based study (15) are promising.

The use of tracer kinetics modeling in the analysis of tomographic images of the prostate is widespread, from the earliest study involving positron emission tomography (PET) (16) through a series of studies involving MR imaging (17–19) and CT (15,20). Although the results of the studies that involved MR imaging indicated that MR imaging has sufficient spatial and contrast resolution to depict cancer, normal peripheral zone tissue, and benign prostatic hyperplasia within individual glands, there is limited information about the microvascular characteristics of these tissues.

Results of studies involving compartmental models have shown that peripheral zone cancers have higher extraction-flow products (transfer constants [K^{trans}]) (21) than normal peripheral zone tissue (17,18). This finding is supported by the generally higher blood flow measured in tumor-containing prostates than in prostates containing benign prostatic hyperplasia alone (16). Differences between tumors and normal tissues that contain benign prostatic hyperplasia are less clear cut in the central portion of the gland, although a recent MR imaging–based study revealed potential differences in flow-related parameters (22). Thus, the purpose of our study was to use contrast-enhanced MR imaging and a distributed-parameter tracer kinetics model for prospectively evaluating the vascular characteristics of prostate cancer.

MATERIALS AND METHODS

Tracer Kinetics Model

There are distinct advantages to employing a distributed-parameter model for analyzing tracer kinetics (23). By definition, compartmental models disregard the tracer's microvascular transit time, and this time is assumed to be negligible on the time scale of typical T1-weighted MR imaging acquisitions. Once the temporal resolution of the experiment is comparable with the transit time, the use of a distributed-parameter model becomes a realistic option (24).

Johnson and Wilson (25) introduced a simple distributed-parameter model in which the internal capillary space contains a tracer, the concentration of which varies in both time and space (along the capillary length). Tracer in the capillary space is in exchange with an external interstitial space that behaves as a well-mixed compartment (ie, there is no spatial variation in tracer concentration). In 1998, St Lawrence and Lee (24) introduced an adiabatic approximation to this model, providing the following time-domain solution suitable for the analysis of imaging data:

$$C_{tis}(t) = F\int_0^{\tau} C_b(t-u)du + EF\int_{\tau}^{t} C_b(u)\exp\left[\frac{-EF(1-\mathrm{hct})}{V_e}(t-u-\tau)\right]du,$$

where C_{tis} and C_b are the concentrations of contrast agent over time, t, in the tissue of interest and blood, respectively; F is the tissue blood flow; hct is the blood hematocrit level; and τ is the mean microvascular transit time, which is equal to the blood volume, V_b, divided by F. V_e is the interstitial tracer distribution volume, and u is a dummy integration variable. The extraction fraction E is calculated with the following equation: $1 - \exp[-PS/F(1 - hct)]$, where PS is the microvascular permeability–surface area product. The product $EF(1 - hct)$ is also referred to as K^{trans} (21).

This model contains four unknown parameters (F, E, V_e, and τ) that may be estimated with curve fitting. From these, the parameters PS and V_b may be evaluated. This model has since been used successfully for the analysis of both MR imaging and CT data (15,26,27).

Patients

Twenty-two consecutive men with histologically proved adenocarcinoma of the prostate who were to be treated with neoadjuvant hormonal treatment and conformal radiation therapy were recruited into this study between June 2001 and February 2003. The local research ethics committee approved the study, and written consent was obtained from all men. Histologic diagnosis was rendered with tissue obtained at transrectal ultrasonographically guided biopsy in 21 men and with tissue obtained at the time of a transurethral resection of the prostate in one man. The clinical stages at presentation were T1c through T3b, with the modal T stage being T3 in 14 patients. All men had had negative results at isotope bone scanning. The mean Gleason score was 6 (range, 5–8), the mean prostate-specific antigen level was 27.5 ng/mL (range, 6–74 ng/mL), and the mean age of the patients was 67 years (range, 57–76 years). After MR imaging and in accordance with local protocol, all men were treated with neoadjuvant hormonal therapy involving a luteinizing hormone–releasing hormone analogue for 3–4 months and three-dimensional conformal radiation therapy.

MR Imaging

MR imaging was performed at 1.5 T (Gyroscan NT/Intera; Philips Medical Systems, Best, the Netherlands) by using a four-element phased-array receiver coil wrapped around the pelvis. These men were expected to undergo follow-up MR imaging after radiation therapy; thus, the use of an endorectal receiver was precluded (28). After the acquisition of scout images, data encompassing the abdomen and pelvis in both the transverse and coronal planes were acquired by using T1-weighted spin-echo sequences. These images were used to assess the possibility of extraprostatic spread. Subsequently, T2-weighted fast spin-echo images of the prostate were obtained in the sagittal and transverse planes with the following parameters: field of view, 200 × 200 mm; section thickness, 3 mm; intersection gap, 0.3 mm; matrix, 256 × 190; repetition time msec/effective echo time msec, 4111/135; echo train length, 19; and number of signals acquired, six. After the acquisition of quantitative data during

contrast agent administration (detailed below), postcontrast T1-weighted spin-echo images of the abdomen and pelvis were again acquired in the transverse plane.

Quantitative data encompassing the pelvic region from the apex of the prostate gland to the bladder were acquired by using a transverse three-dimensional spoiled gradient-echo sequence (ie, a T1-weighted fast-field-echo sequence with an elliptical k-space shutter, a field of view of 300 × 300 × 100 mm, a matrix [after interpolation] of 128 × 128 × 20, and a repetition time msec/echo time msec of 2.5/0.86). Before contrast agent administration, the native T1 relaxation time was mapped by using a series of volume acquisitions (each obtained with four signals acquired) with flip angles of 2°, 10°, 20°, and 30°. After acquisition of the T1 relaxation map data, a dynamic series was acquired by using a 30° flip angle and no averaging over a period of approximately 4 minutes with a total of 100–106 volumes acquired; one volume was acquired every 2.3 seconds. Contrast agent was administered through a cannula that had been placed in the antecubital vein before imaging. After the acquisition of the first five volumes of the dynamic series, 0.1 mmol of gadodiamide (Omniscan; Amersham-Health, Little Chalfont, Buckinghamshire, England) per kilogram of body weight was injected at 3 mL/sec by using an MR imaging–compatible power injector (Spectris; Medrad, Indianola, Pa). The injection of contrast material was immediately followed by injection of a similar volume of normal saline.

Data Collection and Statistical Analysis

Data were transferred off-line for quantitative analysis. For each patient, 4-pixel (22-mm^2) regions of interest were placed (by C.R.) in the external iliac or femoral arteries (to provide a vascular input function). With the aid of the biopsy results and T2-weighted MR images, a radiologist (C.E.H.) also drew regions over muscle (the internal obturator muscle, which was selected as a control tissue) that ranged in size from 148 to 956 mm^2. The radiologist then drew regions over hypointense areas within the peripheral zone that were suspected of containing prostate tumor, and, where possible, regions over normal contralateral peripheral zone tissue. These regions were drawn to encompass as much tumor and normal contralateral peripheral zone as was visible in the selected section. Signal intensity variations in these regions were converted to temporal changes in gadodiamide concentration by using estimates of native T1 calculated by using the precontrast data (29,30).

Finally, the distributed-parameter model described by St Lawrence and Lee (24) was fitted to the data. Multiple fits were performed to each tissue region by using a range of starting points (systematic variation in the initial estimates of τ). The final solution selected was that which minimized the sum of squared differences between the data and the model fit (26,27). To determine whether differences existed between the vascular characteristics of tumor, normal prostate, and muscle in the patients examined, parameter estimates were compared by using the nonparametric Wilcoxon signed rank test (SPSS for Windows, version 11.5; SPSS, Chicago, Ill). $P < .05$ was considered to indicate a statistically significant difference.

RESULTS

MR Imaging

Data were successfully acquired in all 22 patients. Hypointense lesions were outlined in each patient with reference to the T2-weighted MR images and were confirmed with reference to the biopsy reports. Normal-appearing hyperintense regions were further outlined in 20 prostates. Example images and data are presented in Figures 1–3.

Data Analysis

Analysis of the data from the tissue and arterial regions yielded estimates of the relaxation and tracer kinetics parameters. Their mean values ± standard deviations are given in the text below. The native T1 relaxation times of tumor, normal-appearing peripheral zone tissue, and muscle were 916 msec ± 298, 962 msec ± 273, and 1026 msec ± 242, respectively. The model parameter estimates did not follow a normal distribution, and the range and median values for each region and parameter are given in the Table. The mean blood flow in the tumors (66 mL/100 mL/min ± 43) was significantly greater than the mean blood flow measured in normal-appearing peripheral zone tissue (32 mL/100 mL/min ± 36, $P < .001$) and the mean blood flow measured in muscle (9 mL/100 mL/min ± 7, $P < .001$).

Furthermore, the interstitial volume of contrast agent distribution in tumors (42 mL/100 mL ± 20) was larger than both the interstitial volume measured in normal-appearing peripheral zone tissue (27 mL/100 mL ± 10, $P = .003$) and the interstitial volume measured in muscle (12 mL/100 mL ± 17, $P = .002$). The permeability–surface area product of vessels in the tumors (22 mL/100 mL/min ± 12) was similar to that measured in normal-appearing tissue (21 mL/100 mL/min ± 24) but was higher than that measured in muscle (5 mL/100 mL/min ± 5, $P < .001$). These trends were lost for estimates of blood volume, in which significant differences were not seen. Mean blood volume estimates in tumors (1.0 mL/100 mL ± 1.4), normal-appearing peripheral zone tissue (1.5 mL/100 mL ± 2.4), and muscle (1.8 mL/100 mL ± 2.0) were all very low. The mean combined parameter extraction-flow product [$K^{trans}/(1 - hct)$] estimated in tumors (28 mL/100 mL/min ± 13) was significantly greater than that estimated in normal-appearing peripheral zone tissue (15 mL/100 mL/min ± 8, $P < .001$) and in muscle (5 mL/100 mL/min ± 3, $P < .001$).

DISCUSSION

Our findings demonstrate that MR imaging can be used to estimate parameters only previously measured in the prostate gland by using PET (16) or CT (15). These results confirm that blood flow to tumor tissue exceeds that to normal prostatic tissue but that the difference in blood volume is insignificant (16). An increase in the interstitial distribution volume, V_e, has been measured in tumors (18). This may explain the high peak enhancement also measured in tumors (7) and reflect disruption of the epithelial cell layer surrounding prostatic ducts caused by invading cancer cells (31). Unlike in previous studies involving quantitative MR imaging, in the present study, three-dimensional data encompassing the entire prostate gland were acquired. This had the additional advantage of enabling measurement of a vascular input function close to the tissue (30).

Validation

Our estimates of native tissue T1 calculated by using variable-flip-angle three-dimensional gradient-echo acquisitions (29) compare well with previous measurements obtained in both muscle (32) and the prostate (33). Single-capillary distributed-parameter models have previously been used in the analysis of PET

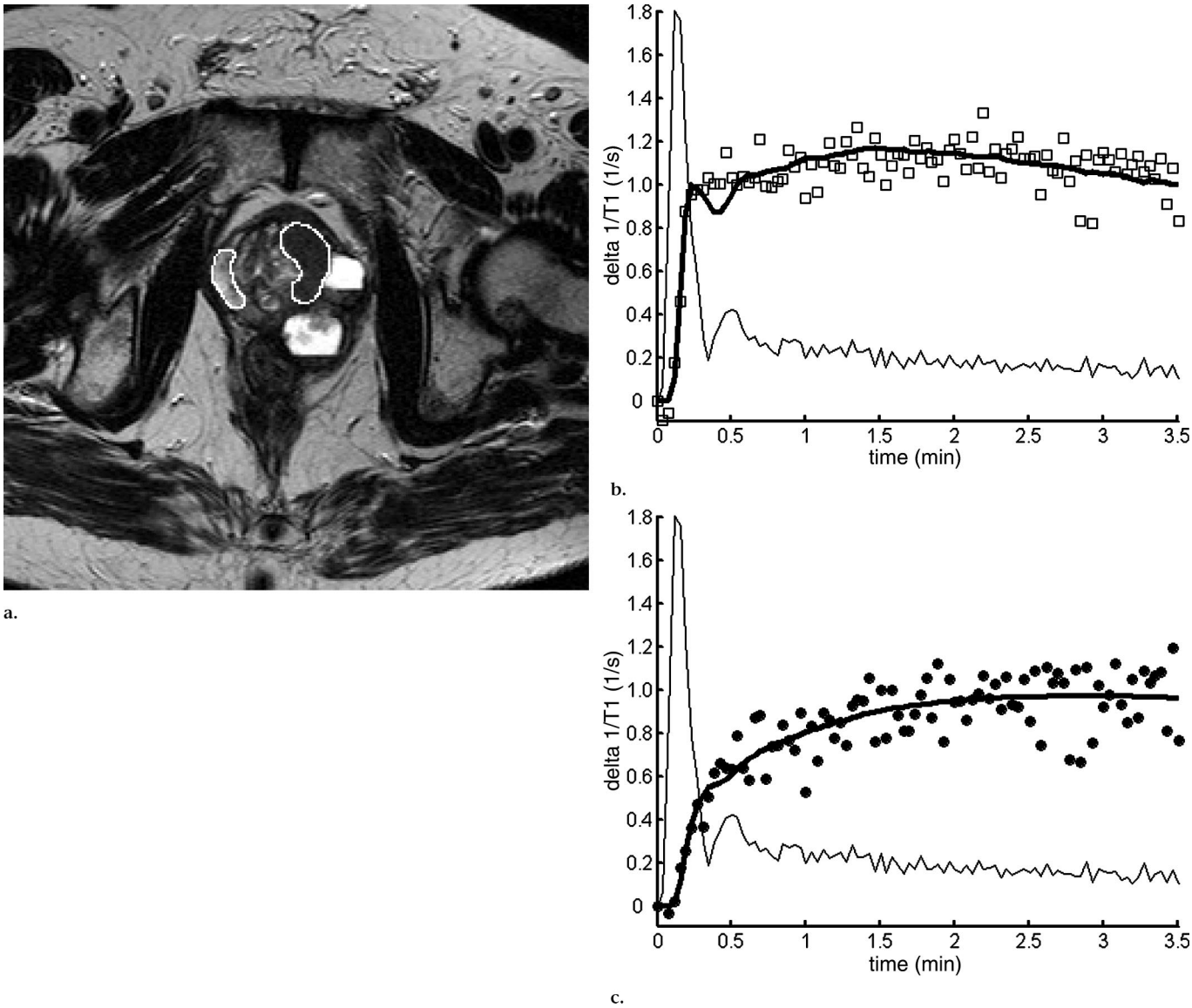

Figure 1. Tissue enhancement in prostate after bolus administration of gadodiamide. **(a)** Transverse T2-weighted turbo spin-echo MR image (4111/135) of prostate gland in 64-year-old man. Regions of interest have been drawn to outline tumor (in left anterior area of prostate) and contralateral normal-appearing peripheral zone tissue (in right side of prostate). **(b, c)** Graphs illustrate enhancement over time in the external iliac artery (thin lines, scaled down by a factor of 10) in **(b)** tumor and **(c)** normal regions. □ and ● = data points. In each graph, the thick line represents the best fit of the model to the data and yields estimates of (among other parameters) blood flow and interstitial distribution volume. In **b**, tumor tissue has a blood flow of 109 mL/100 mL/min and an interstitial distribution volume of 30 mL/100 mL. In **c**, normal tissue has a blood flow of 21 mL/100 mL/min and an interstitial distribution volume of 34 mL/100 mL.

data (23), and the St Lawrence and Lee model specifically has been used in both MR imaging–based studies (26) and CT-based studies (15). Use of a variant of the model for measuring blood flow at CT in comparison with microsphere measurements has been validated in two separate studies (34,35). Although the St Lawrence and Lee model has not yet been formally validated for use in evaluating the prostate, results of simulation studies indicate that this model performs well in comparison to both independent multiple path distributed-parameter models and commonly used compartmental models (27).

In accordance with results of previous work (17,18), the combination of E and F (K^{trans}) measured in the current study was significantly higher in tumor than in normal peripheral zone tissue. The estimates of blood flow in the present study compare well with estimates obtained by using PET (16). Even the small decrease in blood volume that was associated with cancer in our study follows the trend observed in that previous study (16).

Finally, the model-based estimates of blood flow and microvessel permeability–surface area product correlate well with the predictions made by pathologists in previous studies (36). Although tumors contain a greater number of vessels, specifically in angiogenic "hot spots" (8), than do normal tissues, the vessel surface area density in tumors is actually reduced (36). This reflects the size and shape of tumor microvessels, which tend to be broad and less

a.

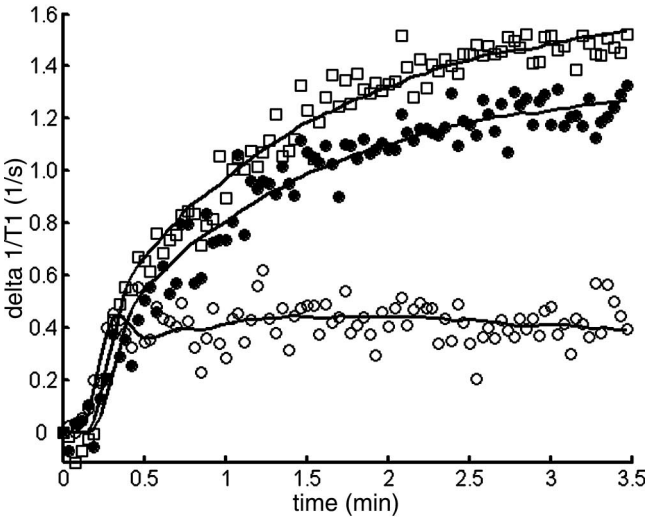

b.

Figure 2. **(a)** Transverse T2-weighted turbo spin-echo MR image (4111/135) obtained in 59-year-old man shows tumor in left posterior area of prostate gland. **(b)** Graph illustrates enhancement over time in tumor (□), normal (●), and muscle (○) regions. The lines represent the best fit of the model to the data. The parameter estimates obtained were as follows: For tumor regions, blood flow was 64 mL/100 mL/min and interstitial distribution volume was 50 mL/100 mL; for normal regions, blood flow was 19 mL/100 mL/min and interstitial distribution volume was 40 mL/100 mL; and for muscle regions, blood flow was 12 mL/100 mL/min and interstitial distribution volume was 7 mL/100 mL.

a.

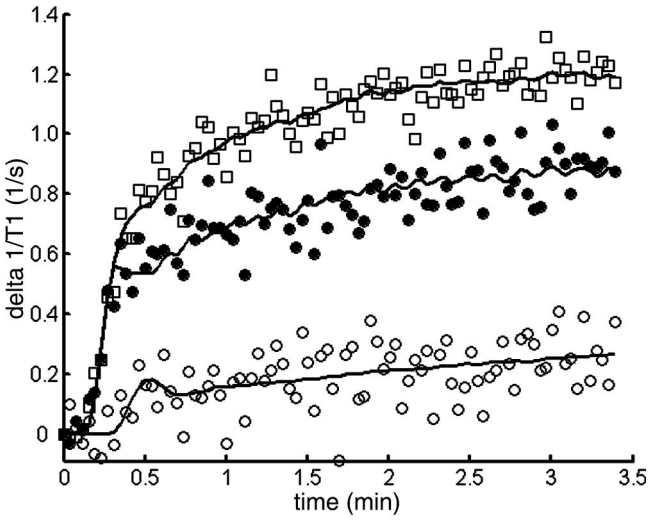

b.

Figure 3. **(a)** Transverse T2-weighted turbo spin-echo MR image (4111/135) obtained in 67-year-old man shows tumor in left posterior area of prostate gland. **(b)** Graph illustrates enhancement over time in tumor (□), normal (●), and muscle (○) regions. The lines represent the best fit of the model to the data. Note the noise in the muscle data and the undulating nature of the model fits that reflect variability in this patient's arterial input function. The parameter estimates obtained were as follows: For tumor regions, blood flow was 132 mL/100 mL/min and interstitial distribution volume was 55 mL/100 mL; for normal regions, blood flow was 109 mL/100 mL/min and interstitial distribution volume was 40 mL/100 mL; and for muscle regions, blood flow was 8 mL/100 mL/min and interstitial distribution volume was 18 mL/100 mL.

branched than those in normal tissue or low-grade tumors. This reduced vessel surface area in high-grade cancers is offset by increased blood flow and vessel wall permeability (36)—physiologic changes that are obscured in the estimate of permeability–surface area product and may explain the similarities between estimates made in tumors and in normal tissue.

Study Limitations

Although concordant imaging and biopsy results provide a highly specific marker of cancer in the peripheral zone (37), this study lacked a standard of reference such as whole-mount prostatectomy specimens (38). Essential to the analysis of any experiment is data quality. The data acquired in the external iliac and femoral arteries and the prostate

Estimates of Blood Flow, Blood Volume, Microvascular Permeability–Surface Area Product, and Interstitial Volume in Prostate Tumors, Normal-appearing Peripheral Zone, and Nearby Muscle

Region	F (mL/100 mL/min)	V_b (mL/100 mL)	PS (mL/100 mL/min)*	V_e (mL/100 mL)
Tumor (n = 22)	57 (30–81)	0.4 (0.2–1.2)	19 (13–32)	38 (27–50)
Normal-appearing tissue (n = 20)	18 (13–32)	0.4 (0.0–2.1)	16 (7–26)	25 (19–34)
Muscle tissue (n = 22)	7 (5–12)	1.2 (0.4–2.6)	5 (2–6)	6 (4–12)

Note.—F = blood flow, PS = microvascular permeability–surface area product, V_b = blood volume, and V_e = interstitial volume. Data are median values. Data in parentheses are interquartile ranges.

* PS could not be determined when the extraction fraction E = 1. PS results are given for 22 tumors, 17 normal-appearing peripheral zones, and 20 areas of nearby muscle.

gland were of good quality, but the signal obtained from the internal obturator muscle was characterized by a poor signal-to-noise ratio and sporadic motion artifacts. Motion interfered with a number of the signal-time courses analyzed, and future studies would probably benefit if image registration was performed before data analysis. The signal-to-noise ratio is conventionally addressed at the expense of temporal resolution.

A reduction in temporal resolution was not an option in the present study because it was necessary to acquire data very rapidly so that a distributed-parameter model could be used. Indeed, the acquisition time that we used was already longer than that recommended in similar studies (39). The limited signal-to-noise ratio is a common problem in prostate MR imaging and may be partly addressed by the use of an endorectal coil (38). Although the use of an endorectal coil is certain to improve the signal from the prostate, it is unlikely to increase the signal from the artery or muscle. Moreover, use of the endorectal coil may be contraindicated in the assessment of patients, such as the patients in our study, who have undergone radiation therapy (28). Alternatively, the signal-to-noise ratio could be improved by using a high-field-strength MR imaging system (40). These limitations may have influenced the accuracy and precision of the parameter estimates that we obtained.

A previous study revealed that estimates of blood volume obtained by using this implementation of the St Lawrence and Lee model were low (27), and the results in the present study fall below previous estimates obtained by using PET (16). This may reflect noise or an inadequate temporal resolution in the experimental data (39) that led to limitations in definition and integration of the arterial input (20). It may also indicate the existence of a limited transendothelial water exchange rate (41,42). The influence of such effects may be reduced by further decreasing the sensitivity of the imaging sequence to water exchange (by increasing the flip angle with so-called exchange minimization [41]). Such an approach further compromises the signal-to-noise ratio of the sequence, and a practical trade-off must be achieved.

Clinical Implications

Our results provide new quantitative physiologic data concerning the prostate gland. These methods, which include measurement of an arterial input function, three-dimensional coverage of the entire prostate gland, and absolute estimates of both flow and permeability–surface area product, represent an advance on those used in previous MR imaging–based studies (7,18). Moreover, similar CT examinations lack tissue coverage (only one or two sections may be examined) and the intrinsic tissue contrast at MR imaging that enables discrimination of tumor from normal peripheral zone tissue (15,20).

These techniques will allow further investigators to characterize tissue types, improve diagnosis, and categorize disease prognosis. The promising results obtained by using qualitative or heuristic methods could be assessed to identify their underlying physiologic basis (7,22). Tissue characterization in the present study was limited by the method of region selection, which was dictated by the patient group examined. Nevertheless, concordant imaging and biopsy results providing a highly specific marker of cancer in the peripheral zone (37) guided selection of prostate tumor regions. Future work would benefit if MR imaging findings were compared with findings in whole-mount prostatectomy specimens, which would constitute an improved standard of reference (38).

Acknowledgments: Jeanette Lyons, Yvonne Watson, and David Clark provided invaluable assistance with the patient studies.

References

1. El-Gabry EA, Halpern EJ, Strup SE, Gomella LG. Imaging prostate cancer: current and future applications. Oncology (Huntingt) 2001; 15:325–336.
2. Schiebler ML, Tomaszewski JE, Bezzi M, et al. Prostatic carcinoma and benign prostatic hyperplasia: correlation of high-resolution MR and histopathologic findings. Radiology 1989; 172:131–137.
3. Mirowitz SA, Brown JJ, Heiken JP. Evaluation of the prostate and prostatic carcinoma with gadolinium-enhanced endorectal coil MR imaging. Radiology 1993; 186:153–157.
4. Brown G, Macvicar DA, Ayton V, Husband JE. The role of intravenous contrast enhancement in magnetic resonance imaging of prostatic carcinoma. Clin Radiol 1995; 50:601–606.
5. Jager GJ, Ruijter ET, van de Kaa CA, et al. Dynamic TurboFLASH subtraction technique for contrast enhanced MR imaging of the prostate: correlation with histopathologic results. Radiology 1997; 203: 645–652.
6. Ogura K, Maekawa S, Okubo K, et al. Dynamic endorectal magnetic resonance imaging for local staging and detection of neurovascular bundle involvement of prostate cancer: correlation with histopathologic results. Urology 2001; 57:721–726.
7. Engelbrecht MR, Huisman HJ, Laheij RJ, et al. Discrimination of prostate cancer from normal peripheral zone and central gland tissue by using dynamic contrast-enhanced MR imaging. Radiology 2003; 229:248–254.
8. Weidner N, Carroll PR, Flax J, Blumenfeld W, Folkman J. Tumor angiogenesis correlates with metastasis in invasive prostate carcinoma. Am J Pathol 1993; 143:401–409.
9. Brawer MK, Deering RE, Brown M, Preston SD, Bigler SA. Predictors of pathological stage in prostatic carcinoma: the role of neovascularity. Cancer 1994; 73:678–687.
10. Lee TY, Purdie TG, Stewart E. CT imaging of angiogenesis. Q J Nucl Med 2003; 47: 171–187.
11. Buckley DL, Drew PJ, Mussurakis S, Monson JR, Horsman A. Microvessel density in invasive breast cancer assessed by dynamic Gd-DTPA enhanced MRI. J Magn Reson Imaging 1997; 7:461–464.

12. Schlemmer HP, Merkle J, Grobholz R, et al. Can pre-operative contrast-enhanced dynamic MR imaging for prostate cancer predict microvessel density in prostatectomy specimens? Eur Radiol 2004; 14: 309–317.
13. Tofts PS. Modeling tracer kinetics in dynamic Gd-DTPA MR imaging. J Magn Reson Imaging 1997; 7:91–101.
14. Bassingthwaighte JB, Goresky CA. Modeling in the analysis of solute and water exchange in the microvasculature. In: Renkin EM, Michel CC, Geiger SR, eds. Handbook of physiology. Section 2: the cardiovascular system. Bethesda, Md: American Physiological Society, 1984; 549–626.
15. Henderson E, Milosevic MF, Haider MA, Yeung IW. Functional CT imaging of prostate cancer. Phys Med Biol 2003; 48: 3085–3100.
16. Inaba T. Quantitative measurements of prostatic blood flow and blood volume by positron emission tomography. J Urol 1992; 148:1457–1460.
17. Turnbull LW, Buckley DL, Turnbull LS, Liney GP, Knowles AJ. Differentiation of prostatic carcinoma and benign prostatic hyperplasia: correlation between dynamic Gd-DTPA enhanced MR imaging and histopathology. J Magn Reson Imaging 1999; 9:311–316.
18. Padhani AR, Gapinski CJ, Macvicar DA, et al. Dynamic contrast enhanced MRI of prostate cancer: correlation with morphology and tumour stage, histological grade and PSA. Clin Radiol 2000; 55:99–109.
19. Muramoto S, Uematsu H, Sadato N, et al. H(2) (15)0 positron emission tomography validation of semiquantitative prostate blood flow determined by double-echo dynamic MRI: a preliminary study. J Comput Assist Tomogr 2002; 26:510–514.
20. Harvey CJ, Blomley MJ, Dawson P, et al. Functional CT imaging of the acute hyperemic response to radiation therapy of the prostate gland: early experience. J Comput Assist Tomogr 2001; 25:43–49.
21. Tofts PS, Brix G, Buckley DL, et al. Estimating kinetic parameters from dynamic contrast-enhanced T1-weighted MRI of a diffusable tracer: standardized quantities and symbols. J Magn Reson Imaging 1999; 10:223–232.
22. Muramoto S, Uematsu H, Kimura H, et al. Differentiation of prostate cancer from benign prostate hypertrophy using dual-echo dynamic contrast MR imaging. Eur J Radiol 2002; 44:52–58.
23. Larson KB, Markham J, Raichle ME. Tracer-kinetic models for measuring cerebral blood flow using externally detected radiotracers. J Cereb Blood Flow Metab 1987; 7:443–463.
24. St Lawrence KS, Lee TY. An adiabatic approximation to the tissue homogeneity model for water exchange in the brain. I. Theoretical derivation. J Cereb Blood Flow Metab 1998; 18:1365–1377.
25. Johnson JA, Wilson TA. A model for capillary exchange. Am J Physiol 1966; 210: 1299–1303.
26. Henderson E, Sykes J, Drost D, Weinmann HJ, Rutt BK, Lee TY. Simultaneous MRI measurement of blood flow, blood volume, and capillary permeability in mammary tumors using two different contrast agents. J Magn Reson Imaging 2000; 12:991–1003.
27. Buckley DL. Uncertainty in the analysis of tracer kinetics using dynamic contrast-enhanced T1-weighted MRI. Magn Reson Med 2002; 47:601–606.
28. Maio A, Rifkin MD. Magnetic resonance imaging of prostate cancer: update. Top Magn Reson Imaging 1995; 7:54–68.
29. Brookes JA, Redpath TW, Gilbert FJ, Murray AD, Staff RT. Accuracy of T1 measurement in dynamic contrast-enhanced breast MRI using two- and three-dimensional variable flip angle fast low-angle shot. J Magn Reson Imaging 1999; 9:163–171.
30. Zhu XP, Li KL, Kamaly-Asl ID, et al. Quantification of endothelial permeability, leakage space, and blood volume in brain tumors using combined T1 and T2* contrast-enhanced dynamic MR imaging. J Magn Reson Imaging 2000; 11:575–585.
31. Noworolski SM, Chen AP, Vigneron DB, Kurhanewicz J. Assessment of prostatic ductal volume using combined dynamic contrast-enhanced MRI and diffusion MRI (abstr). In: Proceedings of the Eleventh Meeting of the International Society for Magnetic Resonance in Medicine. Berkeley, Calif: International Society for Magnetic Resonance in Medicine, 2003; 1464.
32. de Certaines JD, Henriksen O, Spisni A, Cortsen M, Ring PB. In vivo measurements of proton relaxation times in human brain, liver, and skeletal muscle: a multicenter MRI study. Magn Reson Imaging 1993; 11:841–850.
33. Kjaer L, Thomsen C, Iversen P, Henriksen O. In vivo estimation of relaxation processes in benign hyperplasia and carcinoma of the prostate gland by magnetic resonance imaging. Magn Reson Imaging 1987; 5:23–30.
34. Cenic A, Nabavi DG, Craen RA, Gelb AW, Lee TY. A CT method to measure hemodynamics in brain tumors: validation and application of cerebral blood flow maps. AJNR Am J Neuroradiol 2000; 21: 462–470.
35. Purdie TG, Henderson E, Lee TY. Functional CT imaging of angiogenesis in rabbit VX2 soft-tissue tumour. Phys Med Biol 2001; 46:3161–3175.
36. Barth PJ, Weingartner K, Kohler HH, Bittinger A. Assessment of the vascularization in prostatic carcinoma: a morphometric investigation. Hum Pathol 1996; 27:1306–1310.
37. Wefer AE, Hricak H, Vigneron DB, et al. Sextant localization of prostate cancer: comparison of sextant biopsy, magnetic resonance imaging and magnetic resonance spectroscopic imaging with step section histology. J Urol 2000; 164:400–404.
38. Quinn SF, Franzini DA, Demlow TA, Rosencrantz DR, Kim J, Hanna RM. MR imaging of prostate cancer with an endorectal surface coil technique: correlation with whole-mount specimens. Radiology 1994; 190:323–327.
39. Henderson E, Rutt BK, Lee TY. Temporal sampling requirements for the tracer kinetics modeling of breast disease. Magn Reson Imaging 1998; 16:1057–1073.
40. Kim HW, Buckley DL, Peterson DM, et al. In vivo prostate magnetic resonance imaging and magnetic resonance spectroscopy at 3 Tesla using a transceive pelvic phased array coil: preliminary results. Invest Radiol 2003; 38:443–451.
41. Donahue KM, Weisskoff RM, Chesler DA, et al. Improving MR quantification of regional blood volume with intravascular T1 contrast agents: accuracy, precision, and water exchange. Magn Reson Med 1996; 36:858–867.
42. Buckley DL. The influence of transcapillary water exchange on the analysis of tracer kinetics in dynamic Gd-DTPA-enhanced T1-weighted MRI (abstr). In: Proceedings of the Tenth Meeting of the International Society for Magnetic Resonance in Medicine. Berkeley, Calif: International Society for Magnetic Resonance in Medicine, 2002; 2120.